ALE-VMS methods for wind-resistant design of long-span bridges

Tore A. Helgedagsrud[a,*], Yuri Bazilevs[b], Kjell M. Mathisen[a], Ole A. Øiseth[a]

[a]*Department of Structural Engineering, Norwegian University of Science and Technology (NTNU), Richard Birkelands v 1a, NO-7491 Trondheim, Norway*
[b]*School of Engineering, Brown University, 184 Hope Street, Providence, RI 02912, USA*

Abstract

For unsteady aerodynamics, the Arbitrary Lagrangian-Eulerian Variational Multi-Scale (ALE-VMS) formulation for incompressible flows has proven an accurate and powerful method. In this paper we present an overview of some of its applications to wind engineering of long-span bridges, including flutter and buffeting analysis and vortex-induced vibrations. In general the numerical results compare well with the companion wind-tunnel experiments. Further, we use the method to address more special topics of bluff-body aerodynamic; the impact of inlet turbulence on the self-excited forces and the nonconforming span-wise coherence structures of turbulence and buffeting forces. The present work demonstrates the completeness and accuracy of ALE-VMS, and proves it to be a viable engineering tool for bridge aerodynamics.

Keywords: Computational Fluid Dynamics, Fluid-Structure Interaction, Bridge Aerodynamics, Turbulence, Flutter, Buffeting, VIV

*Corresponding author.
Email addresses: tore.a.helgedagsrud@ntnu.no (Tore A. Helgedagsrud), yuri_bazilevs@brown.edu (Yuri Bazilevs), kjell.mathisen@ntnu.no (Kjell M. Mathisen), ole.oiseth@ntnu.no (Ole A. Øiseth)

1. Introduction

The Norwegian Public Roads Administration (NPRA) has initiated a project that aims to construct a continuous connection along the western coast of Norway. The major challenge and cost driver is the seven fjord crossings that span from 1.5 to 5 km, with ferries operating today. For several crossings, single-span suspension bridges are considered the primary option, as the fjords are generally very deep (600 – 1300 m). Adding the strong winds from the North Sea exposure and turbulence-prone terrain, these bridges present engineering challenges that extends far beyond today's technology.

For such long-span bridges, the wind-induced dynamic response is one of the major concerns, and therefore, accurate prediction of the behavior is essential for safe design [1]. This include flutter and buffeting analysis, and vortex-induced vibrations (VIV).

The infamous collapse of the Tacoma Narrows bridge in 1940 marked the starting point, and proved the importance of flutter analysis. This instability phenomenon is driven by the self-excited forces, which may change the properties of the combined wind-structure system such that it not able to dissipate energy and exhibits negative damping [1, 2]. The standard method today is to express the self-excited forces in terms of the so-called aerodynamic derivatives [3] and include them in a modal analysis of the full aeroelastic system [4] or directly in a finite-element analysis [5]. An important factor in non-flutter design is having a high torsional to vertical frequency ratio [6]. For very long spans, this cannot be achieved without an excessive increase in mass, however, it has been shown that a low frequency ratio can be acceptable given a careful design of the aerodynamic properties of the bridge deck [7].

VIV is generated by fluctuating pressure from shedding of vortices in separated flows, and result in a periodic cross-flow excitation. As these approach the eigenfrequencies of the bridge, we get one or more frequency windows in which the vortex shedding synchronizes with the structural vibrations and may result in a relatively significant response [8]. Typically, VIV occurs at low wind speeds and concerns mainly the bridge serviceability. The VIV magnitude is, besides the structural properties, governed by the aerodynamic damping and intensity of the vortex shedding [9]. An effective measure to reduce the latter is installation of devices as guide vanes and fairings, and is utilized on several long-span bridges, e.g., the Hardanger, Storebælt and Osterøy bridge. It is important to consider VIV alongside the flutter analysis due to their interdependence.

Buffeting analysis concerns the turbulence-induced part of the wind actions and may render significant response for an otherwise stable bridge [10], and therefore plays an important role in serviceability and fatigue limit states. Calculation of buffeting response relies on stochastic theory, that was first applied to bridges in [11] and has been further developed into a wide range of methods employed in the frequency domain [4, 10, 12, 13] and time domain [14–17].

Wind-structure interactions have traditionally been subject to wind tunnel experiments. However, as the extremely long bridges will require an extensive aerodynamic analysis, numerical methods based on Computational Fluid Dynamics (CFD) and Fluid-Structure Interaction (FSI) emerge as promising alternatives to reduce the bottleneck of wind tunnel testing. Other advantages of numerical methods are the flexibility of data acquisition, reproducibility and also the possibility to perform full-scale tests and other interaction problems where wind tunnel experiments come short.

Because of the unsteady and dissipative nature of turbulent flows, accurate simulation is extremely difficult and resource intensive. However, with the major development in computational power and technology of the last decades, numerical simulation of turbulent flows have started to find its way into applied bridge engineering, and numerous successful works on flutter analysis, VIV and buffeting are reported in literature.

In the present paper we show applications of CFD and FSI to various aspects of wind-resistant design of bridges using the family of Arbitrary Largrangian-Eulerian Variational Multiscale (ALE-VMS) methods. The ALE-VMS formulation refers to the Residual-Based Variational Multiscale formulation (RBVMS) of the Navier-Stokes equations for incompressible flows [18] extended to moving-domains. Also including the space-time version of RBVMS, referred to as ST-VMS [19], VMS formulations have proven their accuracy and efficiency through numerous high-Reynold-number flow computations, such as parachute FSI [20], wind turbines [21], flapping wings [22], turbo-machinery [23], tire aerodynamics [24], channel flow [25], and also bridge aerodynamics [26–29]. Other key ingredients of the computational framework utilized in this work are the Multi-Domain Modeling (MDM) extension [30, 31] for simulation of incident turbulence, the weakly-enforced boundary conditions [32] for relaxing the no-slip boundary condition at solid surfaces, and Jacobian-based stiffening mesh-moving algorithms [33].

To demonstrate the accuracy and applicability of these methods towards practical wind engineering of bridge structures, we undertake well-known and thoroughly studied bridge sections and present an overview of the major tasks of flutter and buffeting analysis, also studied in our previous works [26–29]. We also

present new results and applications on multi-mode flutter, the impact of incident turbulence on the aerodynamic derivatives, admittance functions, span-wise coherence of turbulence and VIV, some of which related to issues raised in earlier literature.

The paper is outlined as follows. In Sec. 2 we briefly present the general relations of unsteady aerodynamics, to form the point of departure for the numerical applications. A summary of the numerical method is presented in Sec. 3. In Sec. 4, we present the flow computations and numerical results, including comparison with wind-tunnel experiments where applicable. A brief outlook to future opportunities is given in Sec. 5, before the concluding remarks in Sec. 6.

2. Unsteady aerodynamics

With reference to strip theory and the definitions and conventions in Fig. 1, the instantaneous aerodynamic forces on a bridge deck segment subjected to a mean wind component U and zero-mean turbulent fluctuations $\mathbf{u}(x,t) = [u, w]^T$ in the along-wind and vertical directions, respectively, can be represented by the drag, lift and pitching moment: $\mathbf{q}(x,t) = [D, L, M]^T$. Compliant with the in-plane motions, the corresponding displacements are denoted sway, heave and pitching; $\mathbf{d}(x,t) = [p, h, \theta]^T$. In the above, x and t denotes dependency in the span-wise direction and time, respectively.

The drag, lift and pitching moment coefficients per unit length are defined as:

$$C_D = \frac{D}{1/2\rho U^2 H}, \quad C_L = \frac{L}{1/2\rho U^2 B}, \quad C_M = \frac{M}{1/2\rho U^2 B^2}, \tag{1}$$

where ρ is the air density and H and B are the characteristic height and width of the bridge deck, respectively.

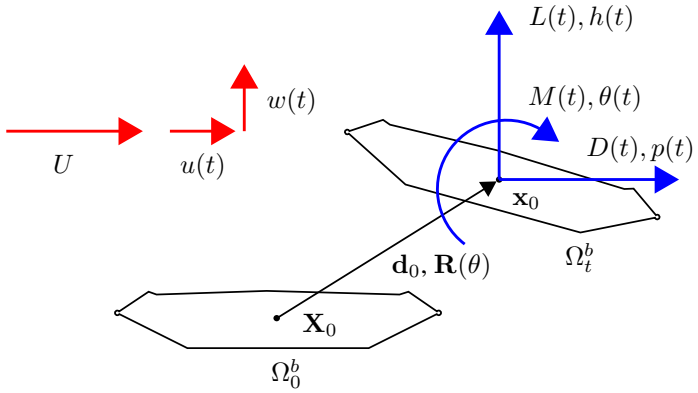

Figure 1: Aerodynamic forces on a moving bridge deck segment subjected to a turbulent wind field and its rigid body kinematics.

For strong winds, we neglect vortex shedding and decompose the aerodynamic forces into mean, self-excited and buffeting components respectively as:

$$\mathbf{q}(x,t) = \overline{\mathbf{q}} + \mathbf{q}_{SE}(x,t) + \mathbf{q}_B(x,t), \tag{2}$$

Using classical multimode theory (see, e.g., [4]) we express the dynamic equilibrium of the bridge in the frequency domain as:

$$\mathbf{M}_0\mathbf{G}_{\ddot{\boldsymbol{\eta}}} + \mathbf{C}_0\mathbf{G}_{\dot{\boldsymbol{\eta}}} + \mathbf{K}_0\mathbf{G}_{\boldsymbol{\eta}} = \mathbf{G}_{\mathbf{q}_{SE}} + \mathbf{G}_{\mathbf{q}_B}, \tag{3}$$

where $\mathbf{M}_0$, $\mathbf{C}_0$ and $\mathbf{K}_0$ are the still-air modal mass, damping and stiffness matrices, respectively, $\mathbf{G}$ denotes the Fourier transform of its attributes $\boldsymbol{\eta}$ and $\mathbf{q}$, that represent the generalized-coordinate parts of $\mathbf{d}$ and $\mathbf{q}$, respectively.

The unsteady self-excited forces may we written in terms of the structural motions as:

$$\mathbf{G}_{\mathbf{q}_{SE}} = \mathbf{C}_{ae}\mathbf{G}_{\dot{\boldsymbol{\eta}}} + \mathbf{K}_{ae}\mathbf{G}_{\boldsymbol{\eta}}, \tag{4}$$

where $\mathbf{C}_{ae}$ and $\mathbf{K}_{ae}$ are interpreted as the aerodynamic damping and stiffness,

respectively, given as:

$$\mathbf{C}_{ae} = \frac{1}{2}\rho U K \begin{bmatrix} P_1^* & P_5^* & BP_2^* \\ H_5^* & H_1^* & BH_2^* \\ BA_5^* & BA_1^* & B^2A_2^* \end{bmatrix}, \tag{5}$$

and

$$\mathbf{K}_{ae} = \frac{1}{2}\rho U^2 K^2 \begin{bmatrix} P_4^* & P_6^* & BP_3^* \\ H_6^* & H_4^* & BH_3^* \\ BA_6^* & BA_4^* & B^2A_3^* \end{bmatrix}. \tag{6}$$

Here, $K = B\omega/U$ is the reduced (angular) frequency and P_i^*,H_i^* and A_i^* are the so-called aerodynamic derivatives [3]. which in general are frequency-dependent functions given by the shape of the bridge.

The critical wind speed for flutter, U^{cr}, is determined by solving the eigenvalue problem of Eq. 3:

$$\left[\lambda_n^2 \mathbf{M}_0 + \lambda_n \left(\mathbf{C}_0 - \mathbf{C}_{ae}\right) + \left(\mathbf{K}_0 - \mathbf{K}_{ae}\right)\right] \mathbf{\Phi}_n = 0. \tag{7}$$

The eigenvalues $\lambda_n = \mu_n \pm i\omega_d$ appear as complex conjugates where the real part corresponds to the decay of mode n and the imaginary part is the damped eigen-frequency. Coupled flutter occurs for the lowest wind speed at which the real part for one of the modes becomes negative. This requires interaction, and shape-wise affinity, between vertical and torsional modes, and are today commonly analyzed in a multimode environment [4, 34].

For the buffeting forces we let $\mathbf{G}_\mathbf{v} = [G_u, G_w]^T$ denote the Fourier transform of the velocity fluctuations. The buffeting can then be given on the following form [1]:

$$\mathbf{G}_{\mathbf{q}_B} = \frac{1}{2}\rho U B \boldsymbol{\chi} \mathbf{G}_\mathbf{v}, \tag{8}$$

where

$$\boldsymbol{\chi} = \begin{bmatrix} 2(H/B)\bar{C}_D\chi_{Du} & ((H/B)C'_D - \bar{C}_L)\chi_{Dw} \\ 2\bar{C}_L\chi_{Lu} & (C'_L + (H/B)\bar{C}_D)\chi_{Lw} \\ 2B\bar{C}_M\chi_{Mu} & BC'_M\chi_{Mw} \end{bmatrix}, \tag{9}$$

is the matrix of aerodynamic admittances. The bars and primes on the force coefficients denote their mean value and inclination with respect to the pitching angle, respectively. Analogue to the aerodynamic derivatives, the admittance functions, χ_{ij}, are frequency-dependent functions governed by the shape of the bridge deck.

The spectral form of Eq. 8 reads:

$$\mathbf{S}_{\mathbf{q}_B} = (\frac{1}{2}\rho UB)^2 \boldsymbol{\chi}\mathbf{S}_{\mathbf{v}}\boldsymbol{\chi}^{*T}, \tag{10}$$

where $\mathbf{S}_{\mathbf{q}_B}$ and $\mathbf{S}_{\mathbf{v}}$ are cross-spectral density matrices of the buffeting forces and wind velocities, respectively. $*T$ denotes the Hermittean transpose of its attribute. Since turbulence is often described in a stochastic sense, Eq. 10 is convenient for response calculations [13] and identification of the admittance functions [35, 36].

In this work, we assume that the cross-spectra of the velocity components, i.e. S_{uw} , S_{wu} are zero, and that C'_D, $\bar{C}_L$ and $\bar{C}_M$ can be neglected. The components of Eq. 10 then reduce to:

$$S_{DD} = \left(\frac{1}{2}\rho UB\right)^2 \left(2\frac{H}{B}\bar{C}_D\right)^2 |\chi_{Du}|^2 S_{uu}, \tag{11a}$$

$$S_{LL} = \left(\frac{1}{2}\rho UB\right)^2 \left(C'_L + \frac{H}{B}\bar{C}_D\right)^2 |\chi_{Lw}|^2 S_{ww}, \tag{11b}$$

$$S_{MM} = \left(\frac{1}{2}\rho UB\right)^2 \left(C'_M\right)^2 |\chi_{Mw}|^2 S_{ww}, \tag{11c}$$

which is recognized as the widely used auto-spectral density method [35].

Vortex-induced vibration typically occurs at lower wind velocities, and is driven by periodic vortex shedding. The vortices create a fluctuating pressure, character-

ized by a dominant shedding frequency $f_s = \mathrm{St}\, U/H$, where St is the Strouhal number. VIV "lock-in" then occurs for ranges of wind speeds where f_s coincides with one of the structural modes, and creates a stable limit-cycle oscillation, often with considerable amplitudes with respect to fatigue and serviceability. VIV is highly dependent on the mass ratio and damping, effectively represented by the Scruton number. For a detailed overview of VIV, the reader is referred to [8].

3. Computational method

3.1. Governing equations

The fluid mechanics is governed by the Navier-Stokes equations of incompressible flows. We take the weak formulation as the starting point, making them suitable for finite element-type discretization. The ALE description makes use of a referential and current fluid mechanics domain, defined by coordinates $\hat{\mathbf{x}} \in \Omega_0$ and $\mathbf{x} \in \Omega_t$, respectively. For the variational formulation, we define the trial and test functional spaces $\mathcal{S}$ and $\mathcal{V}$, respectively, and the problem is stated as follows. Find a velocity-pressure pair $\{\mathbf{v}, p\} \in \mathcal{S}$, such that $\forall\, \{\delta\mathbf{v}, \delta p\} \in \mathcal{V}$:

$$B\left(\{\delta\mathbf{v}, \delta p\}, \{\mathbf{v}, p\}; \hat{\mathbf{v}}\right) - F\left(\{\delta\mathbf{v}, \delta p\}\right) = 0, \tag{12}$$

where

$$\begin{aligned} B(\{\delta\mathbf{v}, \delta p\}, \{\mathbf{v}, p\}; \hat{\mathbf{v}}) = & \\ & \int_{\Omega_t} \delta\mathbf{v} \cdot \rho \left(\left.\frac{\partial \mathbf{v}}{\partial t}\right|_{\hat{x}} + (\mathbf{v} - \hat{\mathbf{v}}) \cdot \boldsymbol{\nabla}\mathbf{v} \right) \mathrm{d}\Omega \\ & + \int_{\Omega_t} \boldsymbol{\varepsilon}(\delta\mathbf{v}) : \boldsymbol{\sigma}(\mathbf{v}, p)\, \mathrm{d}\Omega + \int_{\Omega_t} \delta p \boldsymbol{\nabla} \cdot \mathbf{v}\, \mathrm{d}\Omega, \end{aligned} \tag{13}$$

and

$$F\left(\{\delta\mathbf{v}, \delta p\}\right) = \int_{\Omega_t} \delta\mathbf{v} \cdot \rho\mathbf{f}\, \mathrm{d}\Omega + \int_{(\Gamma_t)_h} \delta\mathbf{v} \cdot \mathbf{h}\, \mathrm{d}\Gamma. \tag{14}$$

Here, ρ is the fluid density, $\mathbf{f}$ is the body forces and $\mathbf{h}$ is the tractions acting on the $(\Gamma_t)_h$ part of the boundary Γ_t. The fluid accelerations is evaluated on Ω_0, denoted by subscript $\hat{x}$, and $\hat{\mathbf{v}} = \partial\hat{\mathbf{x}}/\partial t$ is the fluid domain velocity. $\boldsymbol{\sigma}$ is the Cauchy stress, given as:

$$\boldsymbol{\sigma}(\mathbf{v}, p) = -p\mathbf{I} + 2\mu\,\boldsymbol{\varepsilon}(\mathbf{v}). \tag{15}$$

As stated in Eq. 15, the fluid stresses are defined by an isotropic pressure p, and a viscous part driven by the dynamic viscosity μ and the symmetric strain rate gradient of $\mathbf{u}$, defined as:

$$\boldsymbol{\varepsilon}(\mathbf{v}) = \frac{1}{2}\left(\nabla\mathbf{v} + \nabla\mathbf{v}^T\right). \tag{16}$$

It should be remarked that with the ALE-formulation we still have an Eulerian description of the fluid equations, but at the same time allowing deformation of the fluid mechanics domain without any interaction with the fluid itself.

3.2. Discretization and turbulence modeling

At the discrete level we use standard linear finite elements as well as higher-order accurate isogeometric analysis [37]. The explicit expressions and a comprehensive overview of the methods are given in [38].

For turbulence modeling we use RBVMS [18], which may be regarded as an LES-type model in the sense that it uses the scale separation of resolved and unresolved scales. It differs, however, from classical LES models in that it instead of filtering functions uses a direct-sum decomposition according to the VMS methodology [39] that preserves numerical consistency of the resolved scales in all flow regimes. This was also the motivation for its development in [18, 40]. The term "residual-based" refers to the fact that the discrete point-wise residuals of the strong-form Navier–Stokes equations are used to model the unresolved scales.

The RBVMS is an extension of stabilized methods for fluid mechanics [41], which, through numerous works (see references in [38]) have been developed to render optimal convergence and stability across a wide range of Reynolds numbers.

3.3. Weakly-enforced boundary conditions (BCs)

An important part of the computational framework is the so-called weakly-enforced boundary conditions [32]. Instead of satisfying the Dirichlet boundary conditions exactly, we do so approximately through the variationally consistent penalty terms developed in the framework of Nitsche's method [42]. Although based on numerical considerations, weakly-enforced boundary conditions were shown in [43] to have similarities with near-wall modeling by means of wall functions.

In practice, when the wall boundary layer is under-resolved, the flow is allowed to slip on the solid surface. This avoids formation of artificially thick boundary layers, which often lead to premature flow separation and inaccurate pressure distribution. Weakly-enforced boundary conditions have shown to significantly improve the accuracy and performance, and extended the range of applicability, of RBVMS and ALE-VMS methods, as demonstrated in, e.g., [25, 44].

3.4. Modeling of incident turbulence

Incident turbulence is generated using the MDM-method of [29]. MDM was first proposed in [30] and can be viewed as a generalization of auxiliary recycling methods of which early formulations for turbulence modeling are reported in [45, 46]. As illustrated in Fig. 2, we generate the turbulence separately in

a pressure-driven, wall-bounded channel simulation (Ω^A) with periodic boundary conditions. Its outflow is then imposed as inflow boundary conditions to the main computing domain (Ω^B) that includes a bridge deck. To handle the non-matching discretizations and processor partitioning between the subdomains, we again make use of weakly enforced boundary conditions, which only require quadrature-point inflow-velocity data. The wall boundary conditions of the floor and ceiling is retained in the main computing domain in order to preserve the turbulent structures.

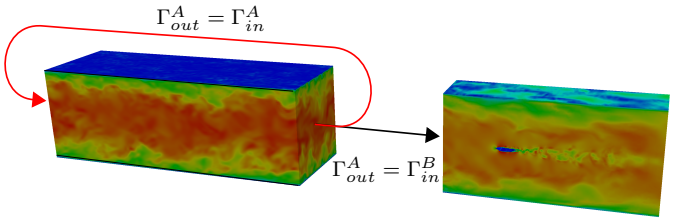

Figure 2: MDM modeling of incident turbulence.

The resulting turbulence proved to render a realistic and high-frequency dissipative velocity spectrum at the position of the bridge deck [29].

3.5. Structural mechanics and FSI

Approaching the bridge deck segment as a rigid object with its initial configuration denoted by Ω^b_0, the dynamic equilibrium state of the object, Ω^b_t, is governed by the global balance of linear and angular momentum stated as:

$$\frac{\mathrm{d}}{\mathrm{d}t}\left(m\mathbf{v}_0\right) + \mathbf{C}^{lin}\mathbf{v}_0 + \mathbf{K}^{lin}\mathbf{d}_0 = \mathbf{F}, \tag{17}$$

and

$$\frac{\mathrm{d}}{\mathrm{d}t}\left(\mathbf{J}_t\boldsymbol{\omega}_0\right) + \mathbf{C}^{ang}\boldsymbol{\omega}_0 + \mathbf{K}^{ang}\boldsymbol{\theta}_0 = \mathbf{M}. \tag{18}$$

In accordance with Fig. 1, $\mathbf{d}_0$ and $\mathbf{v}_0$ are the center-of-mass displacement and velocity, respectively. Similarly, $\boldsymbol{\theta}_0$ and $\boldsymbol{\omega}_0$ are the Euler angle and angular velocity, respectively, $\mathbf{R}(\theta)$ is the rotation matrix, and m and $\mathbf{J}_t$ are the mass and inertia matrix, respectively. Lastly, $\mathbf{C}$ and $\mathbf{K}$ represent the augmented structural damping and stiffness matrices. On the right-hand-side we have the external forces and moments acting on the bridge deck surface, Γ_t^b, given by:

$$\mathbf{F} = m\mathbf{g} + \int_{\Gamma_t^b} \mathbf{h} \mathrm{d}\Gamma, \tag{19}$$

and

$$\mathbf{M} = \int_{\Gamma_t^b} (\mathbf{x} - \mathbf{x}_0) \times \mathbf{h} \mathrm{d}\Gamma, \tag{20}$$

where $\mathbf{g}$ is the gravitational vector and $\mathbf{h}$ are the fluid tractions from Eq. 14. For planar motion, the structural problem reduces to three equations. A detailed view of the discrete formulation is given in [27].

In the case of forced-vibrations, expressions for $\mathbf{d}_0$ and $\boldsymbol{\theta}_0$ are simply given directly.

To conform the fluid mechanics domain to the motion of the bridge, we make use of the fluid mechanics displacement variable $\hat{\mathbf{y}} :\Leftrightarrow \mathrm{d}\hat{\mathbf{y}}/\mathrm{d}t = \hat{\mathbf{v}}$ to solve the linear-elastic equation for the fluid interior. The problem is solved using the interface Γ_t^b as Dirichlet-type boundary conditions, where the elastic constants are given by Jacobian-based stiffening for minimal mesh distortion and wrapping. The method can be viewed in detail in [33].

The resulting FSI equations are solved using a block-iterative coupling and a predictor-multicorrector algorithm based on the Generalized-α time integration method [47]. The discrete FSI equations can be viewed in [38].

3.6. Simulation strategy

Fig. 3 shows the representative 3D CFD finite-element and isogeometric meshes used in this work. Typically, the inflow surface, with prescribed velocity, is placed $3B$ upwind, and the pressure outlet $8B$ downwind. The floor and ceiling is set to the same dimensions as the wind tunnel, with imposed no-penetration and no-slip BCs. The span-wise dimension is set to 0.5 – $2B$ with no-penetration BCs. The bridge segment is extruded through the domain, on which weakly-enforced no-slip is enforced. To better approximate the boundary-layer solution and wake turbulence, prismatic boundary layer elements near the bridge-deck surface, and local wake refinement, are employed.

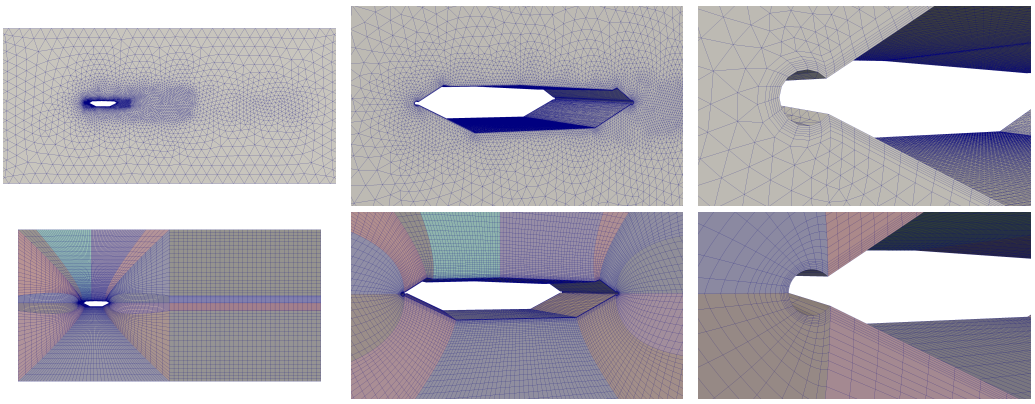

Figure 3: Finite-element (top) and isogeometric (bottom) CFD meshes of the Hardanger bridge.

The air density and dynamic viscosity are set to $\rho = 1.225\ \mathrm{kg/m^3}$ and $\mu = 1.7894 \times 10^{-5}\ \mathrm{kg/ms}$, respectively. The time stepping is chosen such that the maximum Courant number is less than 2.5, typically $\Delta t = 0.001B/U$.

The number of nodes varies from approximately 300×10^3 for higher-order IGA and $500 - 1000 \times 10^3$ for standard finite-elements. A parallel environment is adopted from [48] and the simulations are performed on 256–1024 computational

cores.

4. Numerical simulations

In the following we present the numerical simulations performed and results obtained. The section is divided into flutter, buffeting and VIV analyses presented in Secs. 4.1, 4.2 and 4.3, respectively.

4.1. Flutter analysis

4.1.1. Aerodynamic derivatives and forced-vibrations

The forced-vibration test is an efficient and accurate method to determine the aerodynamic derivatives [49], and from an FSI perspective, also the easiest.

Following the test procedure of [26], the bridge deck is excited in a prescribed harmonic heaving and pitching motion sequentially. From the corresponding measured aerodynamic forces, the aerodynamic derivatives are then estimated by least-squares fitting of Eq. 4. To determine the frequency-dependence of the aerodynamic derivatives, several wind velocities and vibration frequencies are tested.

Fig. 4 shows the resulting aerodynamic derivatives of the Hardanger bridge deck, clean of guide vanes and railings with finite-element and isogeometric discretizations, as reported in [26, 28], respectively. For comparison, results from forced-vibration wind-tunnel experiments [49], are included.

We see that the numerically determined aerodynamic derivatives match the wind-tunnel experiments well, particularly for low values of $U_{red} = 1/K$. In general, the numerical simulations overestimate the force magnitudes. We address this issue in Sec. 4.1.4.

The large deviations in A_4^* arise from a small phase shift in the heaving-induced pitching moment. Note, however, its small amplitude. The impact of

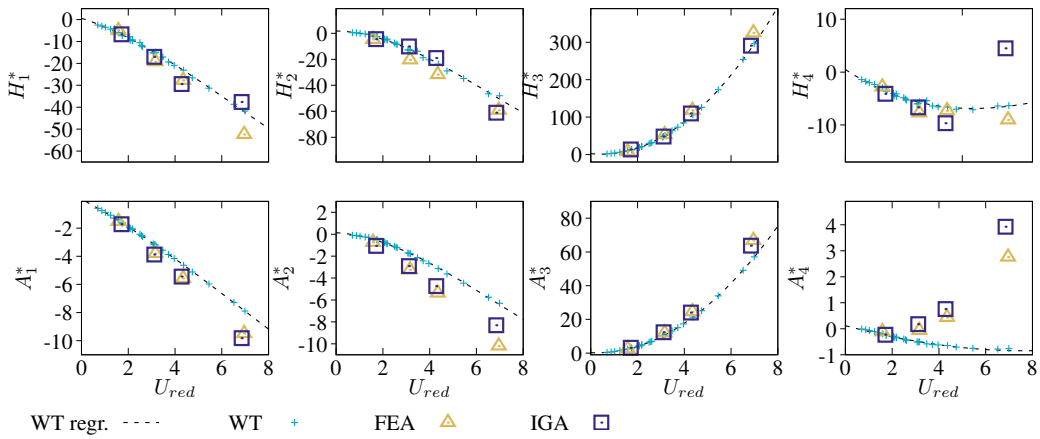

Figure 4: Aerodynamic derivatives of the Hardanger bridge deck obtained by forced-vibration finite-element (FEA) and isogeometric (IGA) analyses and wind-tunnel experiments (WT). Regr. denotes their 3rd order polynomial fitting.

the present aerodynamic derivatives on the flutter characteristics is discussed in Sec. 4.1.3.

The difference between FEA and IGA is only minor and although we see a slight improvement of the heaving phase, the discrepancies do not seem due to the discretization method. It should be remarked, however, that the IGA results were computed with approximately half the number of nodes.

4.1.2. Flutter analysis using free vibrations

For a direct comparison of the flutter characteristics, free-vibration wind-tunnel experiments of the clean Hardanger bridge deck were performed in [27]. Inserting the same still-wind properties into Eqs. 17 and 18, finite-element simulation of flutter is performed for the wind tunnel setup. The results are reported in terms of displacement time series in Fig. 5 and critical velocity and frequency in Tab. 1. The simulation renders a different mean heave, however, in terms of flutter ve-

locity, frequency and mode shape, we capture the experimental results very well.

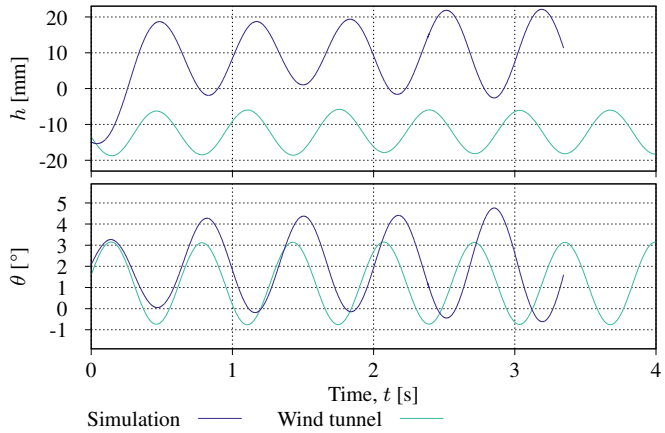

Figure 5: Time series of flutter simulation and companion wind-tunnel experiment.

Remark 1. The flutter simulation in [27] were performed at $U = 8.16$ m/s and showed a rapidly diverging response. The present simulation at $U = 8.10$ m/s shows a much more steady response, suggesting that U_{cr} is very close to 8.1 m/s.

4.1.3. Multimode flutter analysis

To assess the accuracy and impact of the different methods on the flutter characteristics, a multimode flutter computation of the Hardanger bridge is performed using the various aerodynamic derivatives reported in Sec. 4.1.1. We use the same analysis framework and modal quantities as reported in [50], considering the first four symmetrical heaving modes and the first two symmetrical pitching modes and a modal damping of 0.5%. The aerodynamic derivatives are taken as the deck modes of the sectional model, fitted with zero-bounded 3rd order polynomials. For comparison with the free-vibration tests in Sec. 4.1.2, the same computation is also performed for the model scale free-vibration setup, i.e. for bi-modal flutter

with mode shapes of unity. The latter offers a good opportunity for a direct comparison between free- and forced-vibration tests by simulation and wind tunnel experiments.

Table 1: Flutter characteristics of the full-scale Hardanger bridge and a model-scale segment with aerodynamic derivatives determined by experiments and simulations.

Type of test	Full-scale, multi-mode			Model-scale segment		
	U^{cr} [m/s]	ω^{cr} [rad/s]	U^{cr}_{red}	U^{cr} [m/s]	ω^{cr} [rad/s]	U^{cr}_{red}
Wind Tunnel free-vibration	-	-	-	8.16	9.80	2.28
Wind Tunnel forced-vibration	61.41	1.83	1.83	7.80	9.99	2.13
FEA free-vibration	-	-	-	8.10	9.53	2.32
FEA forced-vibration	66.03	1.67	2.16	8.12	9.09	2.44
IGA forced-vibration	65.66	1.67	2.14	8.20	9.15	2.45

The results are summarized in Tab. 1. For both the full- and model scale computation, we see that the simulations produce a higher flutter velocity than the corresponding forced-vibration wind tunnel experiment. Compared to the free-vibration results, however, the simulations predict the flutter behavior with excellent accuracy. Both in terms of the critical velocity and frequency, they match the wind tunnel free-vibration results equally good or better than the companion forced-vibration wind-tunnel experiment, even though the two experiments are preformed in the same wind tunnel, on the same sectional model.

As expected from the similar aerodynamic derivatives, finite-elements and IGA behave more or less equal. Continuing the discussion from Sec. 4.1.1, the results suggest that the deviations from the experimental results is not dominated by the discretization method.

Lastly, we note that the numerical simulations produce more consistent pre-

dictions than those of the wind tunnel, the latter well-known to depend strongly on e.g., the test type [51].

Remark 2. The calculated flutter limit of 61.4 m/s for the Hardanger bridge is far below the design specification. It must be remarked, however, that the present calculations do not include guide vanes, which increases the flutter limit significantly. We also note that the present results correspond well to the flutter calculations in [51].

4.1.4. The role of incident turbulence on aerodynamic derivatives

Consistent for all numerical simulations of self-excited forces on bridges reported in literature known to the authors, is that they overestimate the magnitude of the aerodynamic forces. This is particularly prominent for square cylinders, recognized by their high bluffness and large flow separations, see e.g., [26, 52–54].

It is well-known that incident turbulence reduces the reattachment length of bluff bodies (see e.g., [55, 56]). This was also observed numerically in [29], where early reattachment was found to be more dependent on the existence of incoming turbulence, rather than its intensity. Early reattachment reduces the separation bubble and thus the base suction, which is the governing mechanism for lift and pitching moment. From this observation, the hypothesis of that uniform inflows in numerical simulations contribute to their tendency of overestimating the experiments was proposed, since uniform flows are in practice non-existent, that being in the wind tunnel or in atmospheric flows.

To test this hypothesis, we recalculate the aerodynamic derivatives of the square cylinder of aspect ratio 1:10 (BD10) from [26] with a turbulence intensity

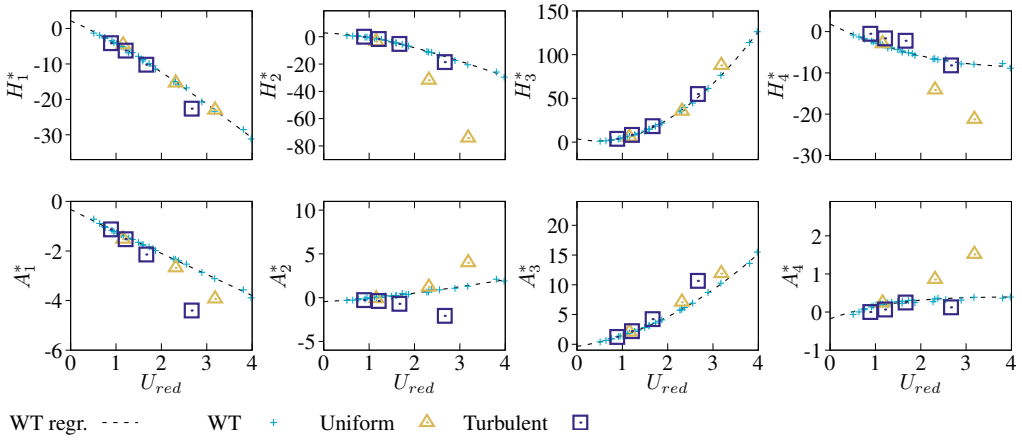

Figure 6: Aerodynamic derivatives for the BD10 section with and without ambient turbulence. The wind tunnel and uniform inflow results are reported in [26].

of 1% in the incoming wind, generally classified as a low intensity. The results are shown in Fig. 6, and compared to the uniform inflow we see a general improvement in terms of the magnitude and particularly the phase of the self-excited forces. The latter is defined from Eq. 4, and given by the ratio between e.g., H_4^* and H_1^* for heaving-induced lift, and has an important impact on the flutter characteristics. Discrepancies are still seen for the pitching moment related terms, in particular A_1^* and A_3^*, however, the overall improvement indicates that inclusion of some perturbations in the incoming wind may have brought the simulation closer to physical flows such as in the wind tunnel through enhanced mixing.

Instant velocity contours at the upper position of the heaving motion for turbulent and uniform inflow are shown in Fig. 7. As seen from the curvature of the shear layer, it is evident that the reattachment length is reduced in the case of turbulent inflow.

Remark 3. The free-stream turbulence intensity of the wind tunnel is approxi-

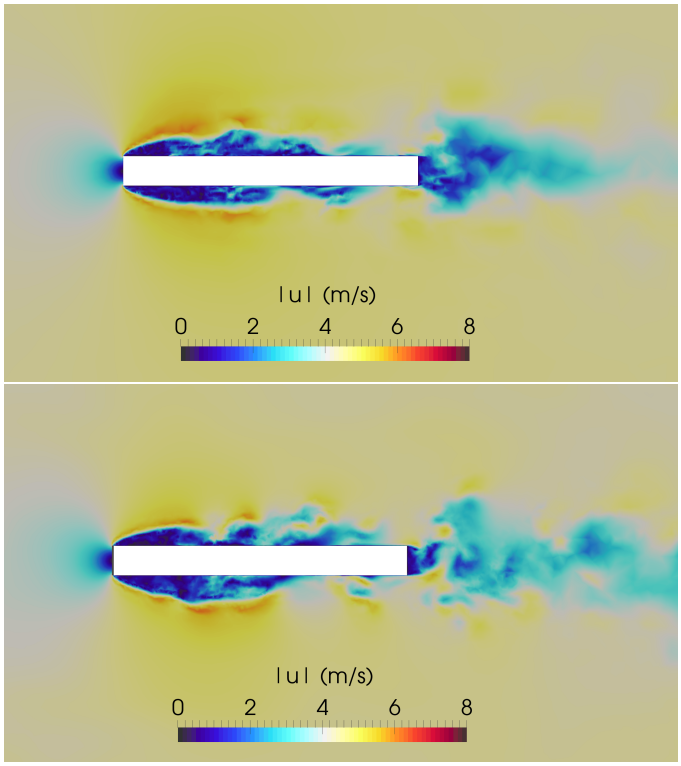

Figure 7: Instant velocity contours of the heaving motion for $U_{red} = 2.7$ at the upper position for uniform (top) and turbulent (bottom) inflow.

mately 0.1%. This would commonly be referred to as a non-turbulent flow in an experimental context.

4.2. Buffeting analysis

4.2.1. Aerdynamic admittance functions

In the study of buffeting, we subject a non-moving bridge section to incident turbulence and use the measured power spectra of the wind velocity and aerodynamic forces to establish the aerodynamic admittance functions (Eq. 11). A detailed description of the method is given in [29], where also admittance functions of the BD10 section was reported. In this work we extend the study to include

the Hardanger bridge section and the NACA0012 airfoil, the latter for comparison with the analytical solution for lifting admittance; The Sears function [57]. To examine the similarity between vertical gust and motions, the aerodynamic admittances based on the experimental aerodynamic derivatives are also computed through the following relations [58]:

$$|\chi^*_{Lw}|^2 = \frac{K^2\left(H_1^{*2} + H_4^{*2}\right)}{C_L'^2} \tag{21}$$

$$|\chi^*_{Mw}|^2 = \frac{K^2\left(A_1^{*2} + A_4^{*2}\right)}{C_M'^2} \tag{22}$$

Figs. 8 and 9 show the aerodynamic admittance functions for lift and pitching moment, respectively. First, we observe that the airfoil follows the Sears function very well, and that the absence of separated flows prevents the high-frequency disturbances. The airfoil solution also appears to be a good approximation for the lifting admittance of the other sections. The increase at high frequencies is induced from shedding of vortices, i.e., the signature turbulence, and is, in that sense, not a part of the buffeting forces. We further notice that the admittances based on aerodynamic derivatives correspond well with the simulations and represent a fair approximation for lift, however, they show a consistently higher admittance.

For the pitching moment, the admittances show a very distinct increase with the bluffness. Although less visible, they also seem to exhibit the same asymptotic behavior of the Sears function, until the signature turbulence becomes dominant. Those based on aerodynamic derivatives indicate a much higher admittance than the simulations, particularly for BD10, exceeding far above unity. This suggests high unsteadiness of the self-excited pitching moment, which makes the conditions that relates aerodynamic derivatives to the admittance function fail. The present observations corresponds very well with those reported in [59].

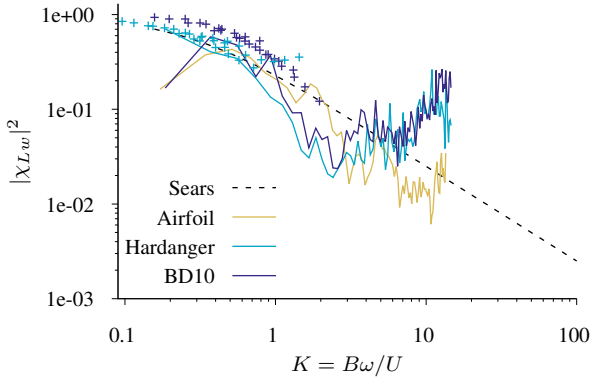

Figure 8: Aerodynamic admittance function for lifting force. The points are admittances computed from experimentally determined aerodynamic derivatives (Eq. (21)).

Remark 4. It should be remarked that the forces are sampled on strips positioned in the middle 1/3 of the domain in order to eliminate any boundary effects near the symmetry planes.

Remark 5. The Sears function is shown with the pitching moment admittances only for visualization. The moments of the airfoil is evaluated about 1/4 of the unit span, with the intention of minimizing the pitching moment, confirmed by its low admittance.

Remark 6. In [29] the signature turbulence was filtered out by subtracting the uniform inflow force spectrum. This step is omitted in the present work, and results in increasing admittances for high frequencies.

4.2.2. Span-wise coherence for isotropic turbulence

In modal analysis of the buffeting response, the span-wise coherence of the buffeting forces must be taken into account. Because such force measurements are lacking, this coherence is modeled using the so-called joint-acceptance function,

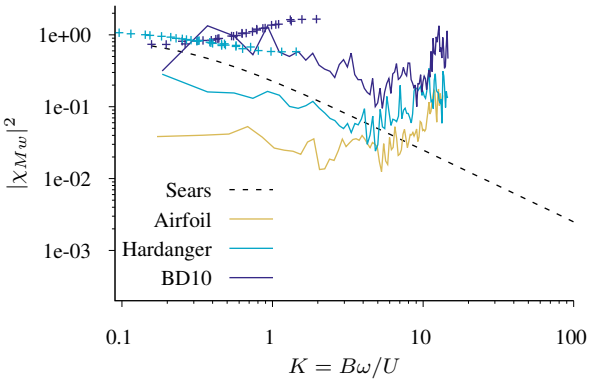

Figure 9: Aerodynamic admittance function for pitching moment.

which is commonly taken as the normalized co-spectrum of the wind field. This assumption is, however, problematic, as it has been suggested that the coherence of the aerodynamic forces is higher than that of the incoming velocity field [60–62].

The normalized co-spectra of the lift and vertical-velocity fluctuations for a span-wise separation Δx are defined, respectively, as:

$$\hat{\mathrm{C}}_L(K, \Delta x) = \frac{\mathrm{Re}\left[S_{L_1 L_2}(K, \Delta x)\right]}{\sqrt{S_{L_1 L_1}(K) \cdot S_{L_2 L_2}(K)}}, \tag{23}$$

$$\hat{\mathrm{C}}_w(K, \Delta x) = \frac{\mathrm{Re}\left[S_{w_1 w_2}(K, \Delta x)\right]}{\sqrt{S_{w_1 w_1}(K) \cdot S_{w_2 w_2}(K)}}. \tag{24}$$

Using the simulation of the BD10 section in Sec. 4.2.1 and measurement strips with separations of $nB/50$, $n = \{1, 2, 4, 8, 16, 32\}$, we compute the normalized co-spectra for the forces and wind fluctuations. For curve fitting we use the extended form of the classical exponential form [63], as used in, e.g., the Hardanger bridge design basis:

$$\hat{\mathrm{C}}_i(K, \Delta x) = \left(1 - \frac{1}{2}\kappa \Delta x\right) \exp\left(-\kappa \Delta x\right), \tag{25}$$

where

$$\kappa = a_i \sqrt{b_i K^2 + c_i}. \tag{26}$$

Fig. 10 shows the normalized lift and velocity co-spectra for separations of $\Delta x = \{B/50, 8B/50, 32B/50\}$ and their fitted curves. Despite the scattered results, partially due to short time series, but also due to the ill-conditioned nature of Eqs. 23 and 24, the trends are clearly visible and well captured by the fitted curves. Figs. 11 and 12 show contours of $\hat{\mathrm{C}}_L(K, \Delta x)$ and $\hat{\mathrm{C}}_w(K, \Delta x)$ for the

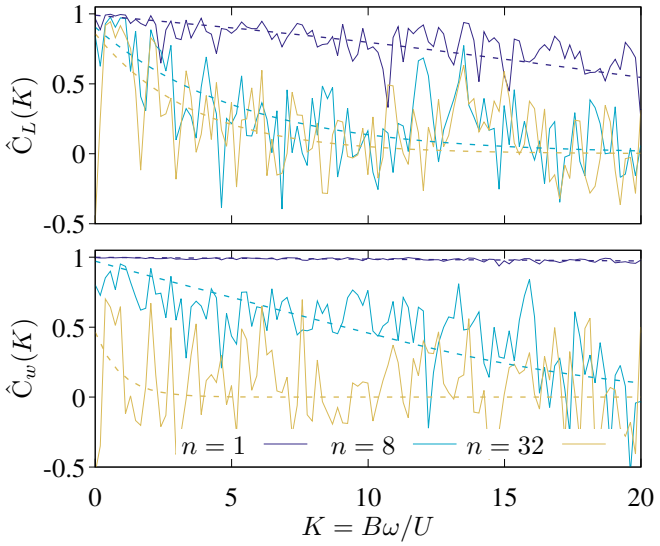

Figure 10: Normalized co-spectra and fitted curves for BD10 lifting force and vertical velocity fluctuations with span-wise separation $nB/50$.

fitted curves of all separations. From these figures it is clearly seen that, for small separations, the wind has a much stronger correlation structure than the forces. A likely explanation is the high vortex intensity, increasing the denominator of Eq. 23 for high reduced frequencies. For separations above $\Delta x/B \approx 0.3$, where the wind correlation drops rapidly, the correlation of the forces remains intact. The latter confirms the observations of [62], and is believed to emerge from constrain-

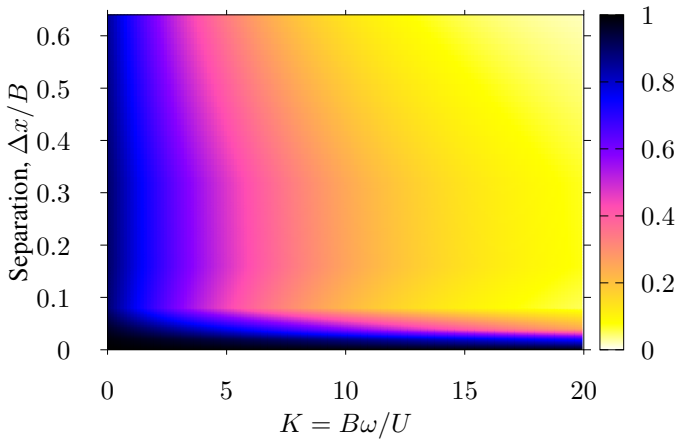

Figure 11: Contours of fitted normalized co-spectra for lifting force, $\hat{\mathrm{C}}_L(K, \Delta x)$, of the BD10 section.

ing the free-stream turbulence. However, the exact mechanism of the dissimilar correlation structures are left for further investigations.

4.3. Vortex-induced vibrations

From a design perspective, VIV of the heaving modes are the main concern, as it occurs for the lowest wind speeds.

To study VIV we use the free-vibration technique from Sec. 3.5. For experimental validation, new wind-tunnel experiments were performed using the same test setup as in [27], except the section was pretensioned vertically in order to increase the stiffness and thus VIV velocity. The identified system properties were $m = 2.91\,\mathrm{kg/m}$, $J_{\theta\theta} = 0.0283\,\mathrm{kgm^2/m}$, $\omega_h = 22.92\,\mathrm{rad/s}$, $\omega_\theta = 66.09\,\mathrm{rad/s}$, with damping ratios of $\zeta_h = 0.225\,\%$ and $\zeta_\theta = 0.1\,\%$. The same structural properties were used as input in the simulations, and subjected to a set of uniform inflow velocities. To trigger the vortices, a small initial displacement of the bridge

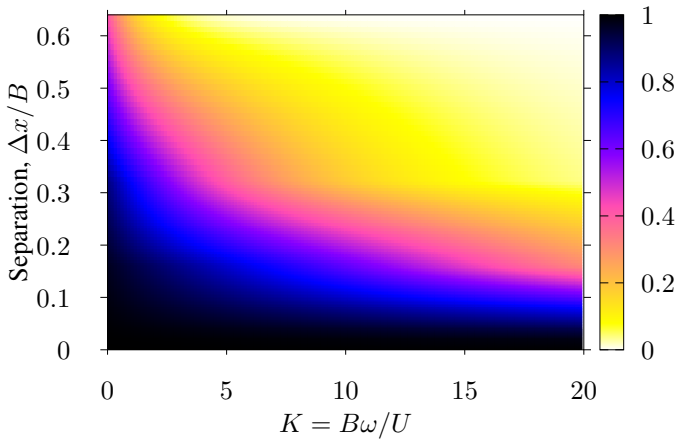

Figure 12: Contours of fitted normalized co-spectra for vertical velocity fluctuation, $\hat{\mathrm{C}}_w(K, \Delta x)$.

deck was set. The VIV magnitude was then taken as the peak displacement of the steady-state, non-decaying, vibration.

Fig. 13 shows the dimensionless displacement as a function of the reduced velocity for the experiments and simulations. Lock-in of the primary peak occurs at reduced velocities $(1/\mathrm{St})$ of approximately 5.6 and 6.0 for the simulation and experiment, respectively. The simulations underestimate the magnitude severely, by almost 50%. A possible explanation arise from the high sensitivity with respect to the domain width of the simulations (B in the present study), indicating that the no-penetration boundary conditions interrupt the formation of fully correlated flows. Another considerable source of error is the system perturbation identification procedure of the still-air properties, due to the ill-conditioned determination of the mass and Scrouton number. Nevertheless, the qualitative trend is well captured, and simulations offer a good opportunity to study the mechanisms of VIV and determine the best countermeasures.

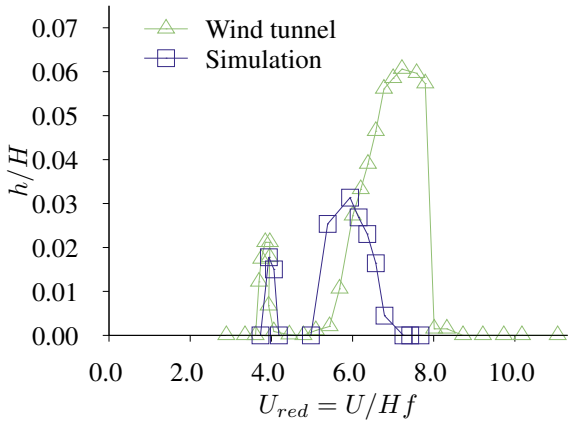

Figure 13: Numerically and experimentally determined VIV in terms of dimensionless displacement and reduced velocity.

The secondary peak appears at approximately $1/1.5\mathrm{St}$ and here, the simulations are in excellent agreement with the experiments.

Remark 7. Due to the multifaceted shape of the Hardanger bridge, its VIV behavior is correspondingly complex. Investigation of the discrepancies seen in this section encourages further investigations, however, preferably on a simpler geometry, e.g., BD10, where the VIV mechanisms can be easier recognized.

5. Outlook

To give the reader an outlook to future applications of ALE-VMS to bridge aerodynamics, we present a full-scale simulation of a low-elevation bridge deck subjected to a “100-year" wind and a bypassing solitary wave. This is an actual load case raised for the Bjørnafjorden crossing, a 4600 m floating bridge and a member of the fjord crossing project.

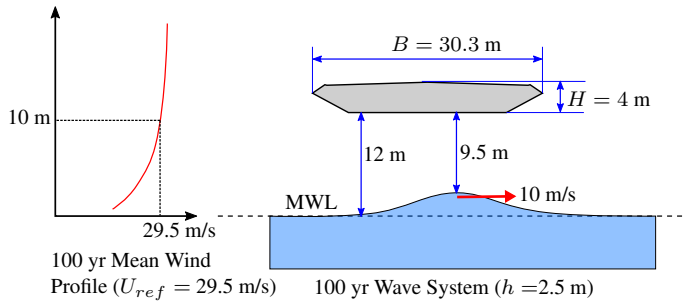

Figure 14: Load case for a low-elevation bridge deck subjected to wind and a bypassing solitary wave.

The load case and dimensions are depicted in Fig. 14. The wave profile is based on the potential flow theory, and is employed by moving the domain floor. The boundary conditions at the floor are imposed weakly and consistently with the air-water interface velocity. The initial position of the wave crest is set to -150 m. A logarithmic wind profile is used at the inlet, with $U = 29.5$ at the reference height of 10 m.

Figs. 15 and 16 show the evolution of lift and pitching moment as a function of the position of the wave crest with respect to the bridge centroid. The same plots also show the average coefficients for still-water, or the hydrostatic condition (MWL), and the same bridge section without the blockage from its low elevation (Free). The simulation reveals a large variation in the forces with respect to the position of the wave and suggests that the sea-state should be considered in the aerodynamic analysis. We also notice that there is a significant increase in the average force coefficients when the blockage is introduced. The plots should be seen in the context of Fig. 17, which shows velocity contours and turbulent structures in terms of the Q-criterion isosurfaces for two positions of the wave. Note how the wind velocity below the bridge deck reduces when the wave is approaching,

and increases when the wave is right below the deck.

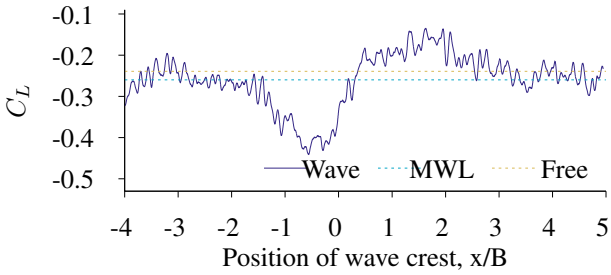

Figure 15: Evolution of lifting force on bridge deck for a bypassing solitary wave.

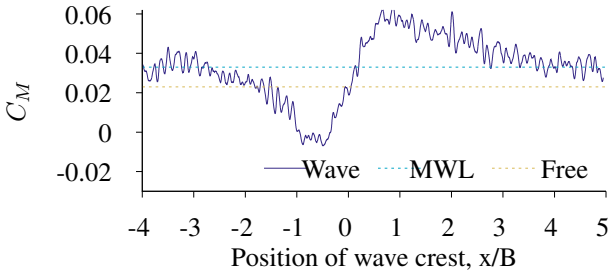

Figure 16: Evolution of pitching moment on bridge deck for a bypassing solitary wave.

It should be remarked that the solitary wave may not be the most realistic sea state. Nevertheless, the present simulation shows the ALE-VMS offers to handle a wide range of wind engineering problems.

6. Conclusions

In this work we apply the ALE-VMS formulation to a wide range of engineering problems within long-span bridge aerodynamics. The formulation combines the advantages of RBVMS turbulence modeling, weakly-enforced boundary conditions, MDM extension for generating inlet turbulence, Jabobian-based stiffening

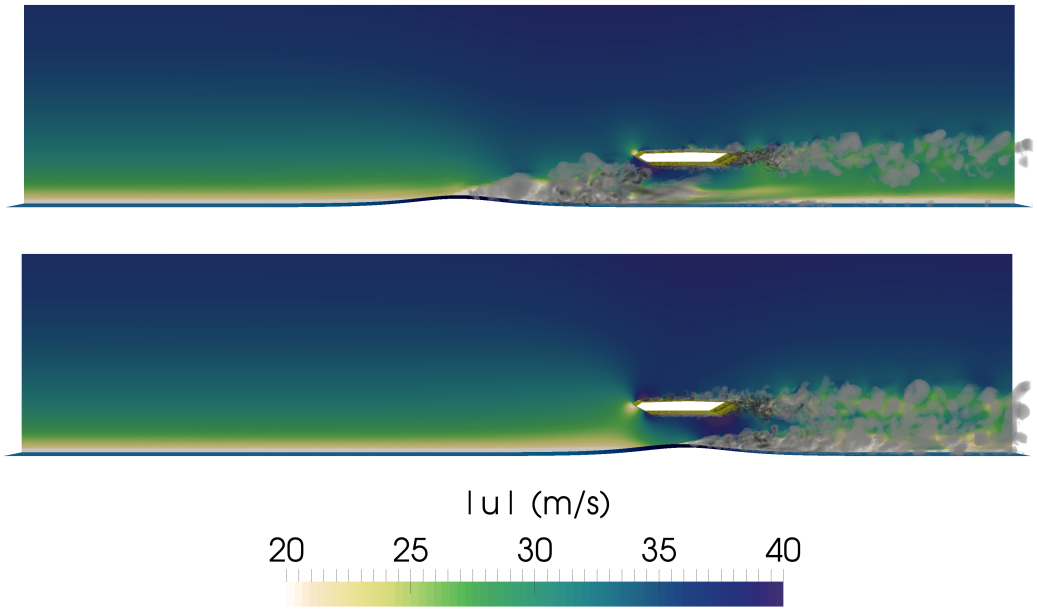

Figure 17: Instant velocity contours and isovolumes of Q-criterion for different positions of the solitary wave.

for mesh-motion and an effective FSI coupling, resulting in a highly developed method for simulation of turbulent flows.

For the flutter analysis we first determined the aerodynamic derivatives for the Hardanger bridge sectional model through forced-vibrations using finite-element and isogeometric distretizations. Both corresponded well with companion wind-tunnel experiments. We also performed numerical and experimental testing of the same section by free-vibrations in order to study the flutter characteristics directly in the time-domain. Numerical simulations of forced- and free-vibrations proved highly consistent and corresponded well to the experiments in terms of the flutter characteristics. The sectional properties were also used as input in a multi-mode flutter analysis of the full-scale bridge for further comparison between

simulations and experiments. The last part of the flutter analysis exploited the hypothesis of that the discrepancies between simulations and experiments may arise from the perfectly uniform inflow conditions commonly used for numerical simulations. Here, we compared the aerodynamic derivatives for the BD10 square cylinder using uniform inflow and inlet turbulence with intensity of 1 %. The results confirmed the importance of incident turbulence on the flow patterns and rendered a general improvement in the phase of the self-excited loads, particularly for the heaving branch.

In the study of buffeting, we computed the aerodynamic admittance function for the BD10, Hardanger bridge and NACA0012 sections. It was found that all sections behaved very similarly to the airfoil for lift, for which also the relation between admittance functions and aerodynamic derivatives was proven to be a fair approximation. The pitching moment admittance showed a strong dependency to the bluffness, but otherwise the same asymptotic behavior. These observations were not captured by the aerodynamic derivative approximation. From the same time series, we further computed the normalized co-spectra of the turbulence and the corresponding buffeting forces. The simulations clearly captured the different correlation structures. The observation is fairly well-known from earlier experiments, however, to the author's knowledge, not captured numerically before.

Lastly, VIV was considered. Free-vibration simulations of the Hardanger bridge sectional model were performed and compared to companion wind-tunnel experiments. The simulations captured the lock-in ranges of the primary and secondary peak with good accuracy, however, the magnitude of the primary peak was severely underestimated. This may have arisen from insufficient width of the computational domain and proximity to the symmetry boundary conditions. For

further VIV simulations we therefore recommend a domain width $> B$.

Through the wide range of bridge aerodynamics problems presented in this work, the ALE-VMS method proves to be an accurate and complete framework for aerodynamic analysis of bridge sections and numerical wind tunnel testing. It also possesses qualities which, in our opinion, makes it viable in the diversity of CFD and FSI methods.

Acknowledgment

This work was carried out with financial support from the Norwegian Public Roads Administration. YB was also partially supported by the NSF Award No. 1854436. All simulations were performed using resources provided by UNINETT Sigma2 - the National Infrastructure for High Performance Computing and Data Storage in Norway. The first author was partially funded by Dr.techn.Olav Olsen AS. The authors greatly acknowledge this support. We would also like to thank Øyving Wiig Petersen and Vegard Antonsen at the Department of Structural Engineering, NTNU, for their help with the VIV wind-tunnel experiments.

References

[1] E. Simiu, R. H. Scanlan, Wind effects on structures : fundamentals and applications to design, 3rd Edition, John Wiley, New York, 1996.

[2] R. Scanlan, The action of flexible bridges under wind, I: Flutter theory, Journal of Sound and Vibration 60 (2) (1978) 187–199. doi:10.1016/S0022-460X(78)80028-5.

[3] R. H. Scanlan, J. Tomko, Airfoil and bridge deck flutter derivatives, Journal of the Engineering Mechanics Division 97 (6) (1971) 1717–1737.

[4] A. Jain, N. P. Jones, R. H. Scanlan, Coupled Flutter and Buffeting Analysis of Long-Span Bridges, Journal of Structural Engineering 122 (7) (1996) 716–725. doi:10.1061/(ASCE)0733-9445(1996)122:7(716).

[5] O. Øiseth, A. Rönnquist, R. Sigbjörnsson, Finite element formulation of the self-excited forces for time-domain assessment of wind-induced dynamic response and flutter stability limit of cable-supported bridges, Finite Elements in Analysis and Design 50 (2012) 173–183. doi:10.1016/j.finel.2011.09.008.

[6] G. Diana, G. Fiammenghi, M. Belloli, D. Rocchi, Wind tunnel tests and numerical approach for long span bridges: The Messina bridge, Journal of Wind Engineering and Industrial Aerodynamics 122 (2013) 38–49. doi:10.1016/j.jweia.2013.07.012.

[7] M. S. Andersen, A. Brandt, Aerodynamic Instability Investigations of a Novel, Flexible and Lightweight Triple-Box Girder Design for Long-Span Bridges, Journal of Bridge Engineering 23 (12) (2018) 04018095. doi:10.1061/(ASCE)BE.1943-5592.0001317.

[8] T. Wu, A. Kareem, An overview of vortex-induced vibration (VIV) of bridge decks, Frontiers of Architecture and Civil Engineering in China 6 (4) (2012) 335–347. doi:10.1007/s11709-012-0179-1.

[9] A. Larsen, J. H. Walther, Aeroelastic Analysis of Bridge Girder Sections based on Discrete Vortex Simulations, Journal of Wind Engineering and Industrial Aerodynamics 67-68 (D) (1997) 253–255. doi:10.1016/S0167-6105(97)00077-9.

[10] A. Fenerci, O. Øiseth, Measured Buffeting Response of a Long-Span Suspension Bridge Compared with Numerical Predictions Based on Design Wind Spectra, Journal of Structural Engineering 143 (9) (2017) 04017131. doi:10.1061/(ASCE)ST.1943-541X.0001873.

[11] A. G. Davenport, Buffeting of a suspension bridge by storm winds, Journal of the Structural Division 88 (3) (1962) 233–270.

[12] R. Scanlan, The action of flexible bridges under wind, II: Buffeting theory, Journal of Sound and Vibration 60 (2) (1978) 201–211. doi:10.1016/S0022-460X(78)80029-7.

[13] X. Chen, M. Matsumoto, A. Kareem, Aerodynamic Coupling Effects on Flutter and Buffeting of Bridges, Journal of Engineering Mechanics 126 (1) (2000) 17–26. doi:10.1061/(ASCE)0733-9399(2000)126:1(17).

[14] X. Chen, M. Matsumoto, A. Kareem, Time Domain Flutter and Buffeting Response Analysis of Bridges, Journal of Engineering Mechanics 126 (1) (2000) 7–16. doi:10.1061/(ASCE)0733-9399(2000)126:1(7).

[15] X. Chen, A. Kareem, Nonlinear response analysis of long-span bridges under turbulent winds, Journal of Wind Engineering and Industrial Aerodynamics 89 (14-15) (2001) 1335–1350. doi:10.1016/S0167-6105(01)00147-7.

[16] L. Caracoglia, N. Jones, Time domain vs. frequency domain characterization of aeroelastic forces for bridge deck sections, Journal of Wind En-

gineering and Industrial Aerodynamics 91 (3) (2003) 371–402. doi:10.1016/S0167-6105(02)00399-9.

[17] C. Costa, C. Borri, O. Flamand, G. Grillaud, Time-domain buffeting simulations for wind–bridge interaction, Journal of Wind Engineering and Industrial Aerodynamics 95 (9-11) (2007) 991–1006. doi:10.1016/j.jweia.2007.01.026.

[18] Y. Bazilevs, V. Calo, J. Cottrell, T. Hughes, A. Reali, G. Scovazzi, Variational multiscale residual-based turbulence modeling for large eddy simulation of incompressible flows, Computer Methods in Applied Mechanics and Engineering 197 (1-4) (2007) 173–201. doi:10.1016/j.cma.2007.07.016.

[19] K. Takizawa, T. E. Tezduyar, Space-Time Fluid-Structure Interaction Methods, Mathematical Models and Methods in Applied Sciences 22 (supp02) (2012) 1230001. doi:10.1142/S0218202512300013.

[20] K. Takizawa, T. E. Tezduyar, C. Boswell, Y. Tsutsui, K. Montel, Special methods for aerodynamic-moment calculations from parachute FSI modeling, Computational Mechanics 55 (6) (2015) 1059–1069. doi:10.1007/s00466-014-1074-5.

[21] Y. Bazilevs, M.-C. Hsu, K. Takizawa, T. E. Tezduyar, ALE-VMS and ST-VMS methods for computer modeling of wind-turbine rotor aerodynamics and fluid-structure interaction, Mathematical Models and Methods in Applied Sciences 22 (supp02) (2012) 1230002. doi:10.1142/S0218202512300025.

[22] K. Takizawa, T. E. Tezduyar, N. Kostov, Sequentially-coupled space–time FSI analysis of bio-inspired flapping-wing aerodynamics of an MAV, Computational Mechanics 54 (2) (2014) 213–233. doi:10.1007/s00466-014-0980-x.

[23] Y. Otoguro, K. Takizawa, T. E. Tezduyar, Space–time VMS computational flow analysis with isogeometric discretization and a general-purpose NURBS mesh generation method, Computers & Fluids 158 (2017) 189–200. doi:10.1016/j.compfluid.2017.04.017.

[24] T. Kuraishi, K. Takizawa, T. E. Tezduyar, Tire aerodynamics with actual tire geometry, road contact and tire deformation, Computational Mechanicsdoi:10.1007/s00466-018-1642-1.

[25] Y. Bazilevs, C. Michler, V. Calo, T. Hughes, Isogeometric variational multiscale modeling of wall-bounded turbulent flows with weakly enforced boundary conditions on unstretched meshes, Computer Methods in Applied Mechanics and Engineering 199 (13-16) (2010) 780–790. doi:10.1016/j.cma.2008.11.020.

[26] T. A. Helgedagsrud, Y. Bazilevs, A. Korobenko, K. M. Mathisen, O. A. Øiseth, Using ALE-VMS to compute aerodynamic derivatives of bridge sections, Computers & Fluids 179 (2019) 820–832. doi:10.1016/j.compfluid.2018.04.037.

[27] T. A. Helgedagsrud, Y. Bazilevs, K. M. Mathisen, O. A. Øiseth, Computational and experimental investigation of free vibration and flutter of

bridge decks, Computational Mechanics 63 (1) (2019) 121–136. doi:10.1007/s00466-018-1587-4.

[28] T. A. Helgedagsrud, I. Akkerman, Y. Bazilevs, K. M. Mathisen, O. A. Øiseth, Isogeometric Modeling and Experimental Investigation of Moving-Domain Bridge Aerodynamics, Journal of Engineering Mechanics 145 (5) (2019) 04019026. doi:10.1061/(ASCE)EM.1943-7889.0001601.

[29] T. A. Helgedagsrud, Y. Bazilevs, K. M. Mathisen, J. Yan, O. A. Øseth, Modeling and simulation of bridge-section buffeting response in turbulent flow, Mathematical Models and Methods in Applied Sciences (2019) 1–28doi:10.1142/S0218202519410045.

[30] Y. Osawa, T. Tezduyar, 3D simulation and visualization of unsteady wake flow behind a cylinder, Journal of Visualization 2 (2) (1999) 127–134. doi:10.1007/BF03181515.

[31] Y. Bazilevs, J. Yan, M. de Stadler, S. Sarkar, Computation of the Flow Over a Sphere at Re = 3700: A Comparison of Uniform and Turbulent Inflow Conditions, Journal of Applied Mechanics 81 (12) (2014) 121003. doi:10.1115/1.4028754.

[32] Y. Bazilevs, C. Michler, V. M. Calo, T. J. R. Hughes, Weak Dirichlet boundary conditions for wall-bounded turbulent flows, Computer Methods in Applied Mechanics and Engineering 196 (49-52) (2007) 4853–4862. doi:10.1016/j.cma.2007.06.026.

[33] K. Stein, T. Tezduyar, R. Benney, Mesh Moving Techniques for Fluid-

Structure Interactions With Large Displacements, Journal of Applied Mechanics 70 (1) (2003) 58. doi:10.1115/1.1530635.

[34] T. Agar, Aerodynamic flutter analysis of suspension bridges by a modal technique, Engineering Structures 11 (2) (1989) 75–82. doi:10.1016/0141-0296(89)90016-3.

[35] G. L. Larose, Experimental determination of the aerodynamic admittance of a bridge deck segment, Journal of Fluids and Structures 13 (7-8) (1999) 1029–1040. doi:10.1006/jfls.1999.0244.

[36] L. Zhu, Q. Zhou, Q. Ding, Z. Xu, Identification and application of six-component aerodynamic admittance functions of a closed-box bridge deck, Journal of Wind Engineering and Industrial Aerodynamics 172 (November 2017) (2018) 268–279. doi:10.1016/j.jweia.2017.11.002.

[37] J. A. Cottrell, T. J. R. Hughes, Y. Bazilevs, Isogeometric Analysis, John Wiley & Sons, Ltd, Chichester, UK, 2009. doi:10.1002/9780470749081.

[38] Y. Bazilevs, K. Takizawa, T. E. Tezduyar, Computational Fluid-Structure Interaction, John Wiley & Sons, Ltd, Chichester, UK, 2013. doi:10.1002/9781118483565.

[39] T. J. R. Hughes, G. Scovazzi, L. P. Franca, Multiscale and Stabilized Methods, in: Encyclopedia of Computational Mechanics Second Edition, John Wiley & Sons, Ltd, Chichester, UK, 2017, pp. 1–64. doi:10.1002/9781119176817.ecm2051.

URL http://doi.wiley.com/10.1002/9781119176817.ecm2051

[40] T. J. Hughes, L. Mazzei, K. E. Jansen, Large Eddy Simulation and the variational multiscale method, Computing and Visualization in Science 3 (1-2) (2000) 47–59. doi:10.1007/s007910050051.

[41] A. N. Brooks, T. J. R. Hughes, Streamline upwind/Petrov-Galerkin formulations for convection dominated flows with particular emphasis on the incompressible Navier-Stokes equations, Computer Methods in Applied Mechanics and Engineering 32 (1-3) (1982) 199–259. doi:10.1016/0045-7825(82)90071-8.

[42] J. Nitsche, Über ein Variationsprinzip zur Lösung von Dirichlet-Problemen bei Verwendung von Teilräumen, die keinen Randbedingungen unterworfen sind, Abhandlungen aus dem Mathematischen Seminar der Universität Hamburg 36 (1) (1971) 9–15. doi:10.1007/BF02995904.

[43] Y. Bazilevs, T. J. R. Hughes, Weak imposition of Dirichlet boundary conditions in fluid mechanics, Computers and Fluids 36 (1) (2007) 12–26. doi:10.1016/j.compfluid.2005.07.012.

[44] M.-C. Hsu, I. Akkerman, Y. Bazilevs, Wind turbine aerodynamics using ALE–VMS: validation and the role of weakly enforced boundary conditions, Computational Mechanics 50 (4) (2012) 499–511. doi:10.1007/s00466-012-0686-x.

[45] T. S. Lund, P. Moin, Large-eddy simulation of a concave wall boundary

layer, International Journal of Heat and Fluid Flow 17 (3) (1996) 290–295. doi:10.1016/0142-727X(96)00039-2.

[46] Y. M. Chung, H. J. Sung, Comparative Study of Inflow Conditions for Spatially Evolving Simulation, AIAA Journal 35 (2) (1997) 269–274. doi:10.2514/2.117.

[47] K. E. Jansen, C. H. Whiting, G. M. Hulbert, A generalized-α method for integrating the filtered Navier–Stokes equations with a stabilized finite element method, Computer Methods in Applied Mechanics and Engineering 190 (3-4) (2000) 305–319. doi:10.1016/S0045-7825(00)00203-6.

[48] M.-C. Hsu, I. Akkerman, Y. Bazilevs, High-performance computing of wind turbine aerodynamics using isogeometric analysis, Computers & Fluids 49 (1) (2011) 93–100. doi:10.1016/j.compfluid.2011.05.002.

[49] B. Siedziako, O. Øiseth, An enhanced identification procedure to determine the rational functions and aerodynamic derivatives of bridge decks, Journal of Wind Engineering and Industrial Aerodynamics 176 (2018) 131–142. doi:10.1016/j.jweia.2018.03.025.

[50] O. Øiseth, A. Rönnquist, R. Sigbjörnsson, Simplified prediction of wind-induced response and stability limit of slender long-span suspension bridges, based on modified quasi-steady theory: A case study, Journal of Wind Engineering and Industrial Aerodynamics 98 (12) (2010) 730–741. doi:10.1016/j.jweia.2010.06.009.

[51] B. Siedziako, O. Øiseth, On the importance of cross-sectional details in the

wind tunnel testing of bridge deck section models, Procedia Engineering 199 (2017) 3145–3151. doi:10.1016/j.proeng.2017.09.573.

[52] S. de Miranda, L. Patruno, F. Ubertini, G. Vairo, On the identification of flutter derivatives of bridge decks via RANS turbulence models: Benchmarking on rectangular prisms, Engineering Structures 76 (2014) 359–370. doi:10.1016/j.engstruct.2014.07.027.

[53] R. Scotta, M. Lazzari, E. Stecca, J. Cotela, R. Rossi, Numerical wind tunnel for aerodynamic and aeroelastic characterization of bridge deck sections, Computers and Structures 167 (2016) 96–114. doi:10.1016/j.compstruc.2016.01.012.

[54] F. Brusiani, S. D. Miranda, L. Patruno, F. Ubertini, P. Vaona, On the evaluation of bridge deck flutter derivatives using RANS turbulence models, Journal of Wind Engineering 119 (2013) 39–47.

[55] Y. Nakamura, Y. Ohya, S. Ozono, The effects of turbulence on bluff-body mean flow, Journal of Wind Engineering and Industrial Aerodynamics 28 (1-3) (1988) 251–259. doi:10.1016/0167-6105(88)90121-3.

[56] R. Mills, J. Sheridan, K. Hourigan, Response of base suction and vortex shedding from rectangular prisms to transverse forcing, Journal of Fluid Mechanics 461 (2002) 25–49. doi:10.1017/S0022112002008534.

[57] W. R. Sears, Some Aspects of Non-Stationary Airfoil Theory and Its Practical Application, Journal of the Aeronautical Sciences 8 (3) (1941) 104–108. doi:10.2514/8.10655.

[58] R. H. Scanlan, Motion-Related Body-Force Functions in Two-Dimensional Low-Speed Flow, Journal of Fluids and Structures 14 (1) (2000) 49–63. doi:10.1006/jfls.1999.0252.

[59] C. Costa, Aerodynamic admittance functions and buffeting forces for bridges via indicial functions, Journal of Fluids and Structures 23 (3) (2007) 413–428. doi:10.1016/j.jfluidstructs.2006.10.002.

[60] G. L. Larose, J. Mann, Gust loading on streamlined bridge decks, Journal of Fluids and Structures 12 (5) (1998) 511–536. doi:10.1006/jfls.1998.0161.

[61] J. Bogunovic Jacobsen, Fluctuating wind load and response of a line-like engineering structure with emphasis on motion-induced wind forces, Phd thesis, The Norwegian Institute of Technology, Trondheim, Norway (1995).

[62] Y. Ito, H. Shirato, M. Matsumoto, Coherence characteristics of fluctuating lift forces for rectangular shape with various fairing decks, Journal of Wind Engineering and Industrial Aerodynamics 135 (2014) 34–45. doi:10.1016/j.jweia.2014.10.003.

[63] S. Krenk, IUTAM Symposium on Advances in Nonlinear Stochastic Mechanics, in: A. Naess, S. Krenk (Eds.), IUTAM Symposium on Advances in Nonlinear Stochastic Mechanics, Vol. 47 of Solid Mechanics and its Applications, Springer Netherlands, Dordrecht, 1996, pp. 269–278. doi:10.1007/978-94-009-0321-0.